

A framework for organ dose estimation in x-ray angiography and interventional radiology based on dose-related data in DICOM structured reports

Artur Omar^{1,2}, Robert Bujila^{1,3}, Annette Fransson¹, Pedro Andreo¹ and Gavin Poludniowski^{1,2}

¹ Department of Medical Physics, Karolinska University Hospital, SE-171 76 Stockholm, Sweden

² Department of Oncology-Pathology, Karolinska Institutet, SE-171 76 Stockholm, Sweden

³ Department of Physics, Royal Institute of Technology, SE-106 91 Stockholm, Sweden

E-mail: artur.omar@karolinska.se

Abstract. Although interventional x-ray angiography (XA) procedures involve relatively high radiation doses that can lead to deterministic tissue reactions in addition to stochastic effects, convenient and accurate estimation of absorbed organ doses has traditionally been out of reach. This has mainly been due to the absence of practical means to access dose-related data that describe the physical context of the numerous exposures during an XA procedure. The present work provides a comprehensive and general framework for the determination of absorbed organ dose, based on non-proprietary access to dose-related data by utilizing widely available DICOM radiation dose structured reports (RDSR). The framework comprises a straightforward calculation workflow to determine the incident kerma and reconstruction of the geometrical relation between the projected x-ray beam and the patient's anatomy. The latter is difficult in practice, as the position of the patient on the table top is unknown. A novel patient-specific approach for reconstruction of the patient position on the table is presented. The proposed approach was evaluated for 150 patients by comparing the estimated position of the primary irradiated organs (the target organs) with their position in clinical DICOM images. The approach is shown to locate the target organ position with a mean (max) deviation of 1.3 (4.3), 1.8 (3.6) and 1.4 (2.9) cm for neurovascular, adult and paediatric cardiovascular procedures, respectively. To illustrate the utility of the framework for systematic and automated organ dose estimation in routine clinical practice, a prototype implementation of the framework with Monte Carlo simulations is included.

PACS numbers: 87.53.Bn, 87.57.uq, 87.59.Dj

Submitted to: *Phys. Med. Biol.*

1. Introduction

Although medical imaging provides considerable improvements in the diagnosis and treatment of a wide range of medical conditions, the radiation dose from x-ray examinations is of concern. Some types of examinations, such as interventional x-ray angiography (XA) procedures, involve relatively high radiation doses that can lead to deterministic tissue reactions in addition to stochastic effects (ICRP, 2012). Over the last decade, the individual patient's exposure from radiological procedures has steadily been increasing. This has primarily been due to an increased number of radiological procedures, which in XA has been spurred by rapid advances in minimally invasive techniques and technologies for image guidance, a trend that is likely to continue in the future (Kagadis et al., 2012). To mitigate the risk of unnecessary radiation exposure, and to provide data for decision support in justification and optimization, patient radiation dose tracking is considered to be of crucial importance. The importance of recording, reporting and tracking patients' exposures was emphasized in a joint position statement issued by several international organizations in 2012 (IAEA, 2012).

Even though the importance of accurate patient dosimetry is well known, convenient, expeditious, and accurate estimation of absorbed (or equivalent) organ dose has traditionally not been possible for XA procedures. The most accurate method has consisted of tedious clinical measurements to determine the dose delivered to superficial organs such as the skin, the thyroid gland and the lens of the eye (e.g. Vano et al., 2001; Theodorakou and Horrocks, 2003). Alternative methods have been employed based on the use of precalculated Monte Carlo (MC) factors and coefficients (McCullough and Schueler, 2000; Schlattl et al., 2007; Benmakhlouf et al., 2011, 2013) for the determination of absorbed dose to internal organs and to the skin. These methods rely on dose-related data that describe the physical context of the individual exposures of the performed XA procedure to generate an accurate dose estimate. Such data has not been readily available in the past; consequently MC based methods have been associated with a large uncertainty. Therefore, dosimetry of internal organs has traditionally been limited to the estimation of effective dose using coefficients converting cumulative (over an entire procedure) dose indices of air kerma-area product, P_{KA} (IAEA, 2009; NCRP, 2009). These kinds of coefficients are cumbersome to determine and are limited to specific clinical situations (ICRU, 2006). Moreover, such coefficients are not suitable for the estimation of absorbed organ dose, as cumulative dose indices are poorly correlated to absorbed dose if the patient size and the specific clinical examination technique are not taken into account (Miller et al., 2003; Karambatsakidou et al., 2005; Compagnone et al., 2011).

A small number of applications to estimate patient skin dose (den Boer et al., 2001; Chugh et al., 2004) have been developed based on the extraction of dose-related data directly from specific XA systems. Unfortunately, as the developed applications rely heavily upon proprietary access to relevant information, a widespread clinical implementation is impeded. This issue was addressed with supplement 94 to

the DICOM Standard, which introduced diagnostic x-ray radiation dose structured reporting (RDSR) (DICOM, 2005) to support convenient and non-proprietary access to dose-related data. Despite the fact that RDSR has become widely used and also has the potential to greatly improve the accuracy of patient dose estimations for radiological procedures, the availability of organ dose applications is scarce. Khodadadegan et al. (2011) was the first group to develop a method for systematic estimation of patient skin dose from XA procedures using RDSR. Shortly thereafter, Johnson et al. (2011a) proposed a similar method for real-time skin dose mapping, with in-clinic anthropometric measurements for patient-phantom size matching. The described applications use methods that have been developed specifically for estimation of patient skin dose. To our knowledge there has been no method developed for estimation of dose to organs other than the skin.

The aim of the present work is to provide a rigorous and general framework for the determination of absorbed organ dose in XA, based on the dose-related data contained in RDSR. A novel patient-specific method for reconstruction of the geometrical alignment of the patient's anatomy with the projected x-ray beam is emphasized. Lastly, a prototype implementation of the proposed framework combined with the MC method is demonstrated to illustrate the utility of the framework for organ dose estimations in routine clinical practice.

2. Methods and materials

2.1. Framework for the determination of absorbed organ dose

To estimate the absorbed dose to internal organs and to the skin from XA procedures based on the information available in the RDSR, a comprehensive and general framework was established as outlined in this section. The framework comprises the calculation workflow illustrated in figure 1, which consists of three conceptually distinct parts:

- Calculation of the incident kerma in a scatter-free geometry (free-in-air).
- Reconstruction of the geometrical relation between the projected x-ray beam and the patient's anatomy.
- Conversion of the calculated incident kerma to absorbed organ dose, considering both the primary component and scattering processes in the patient.

RDSR dose-related data is used for the calculation of the incident kerma, and for the alignment of the geometry of the projected x-ray beam with a phantom model that represents the patient anatomy, i.e. patient-phantom matching. The final step consists in the calculation of the absorbed dose by connecting the framework to a general purpose MC code, a particular purpose-specific MC software, or a code implementing conversion factors. The framework provides a general approach for utilizing dose-related data contained in RDSR for patient dosimetry, allowing any type of phantom model and method for radiation transport in the phantom to be used in connection with it. The

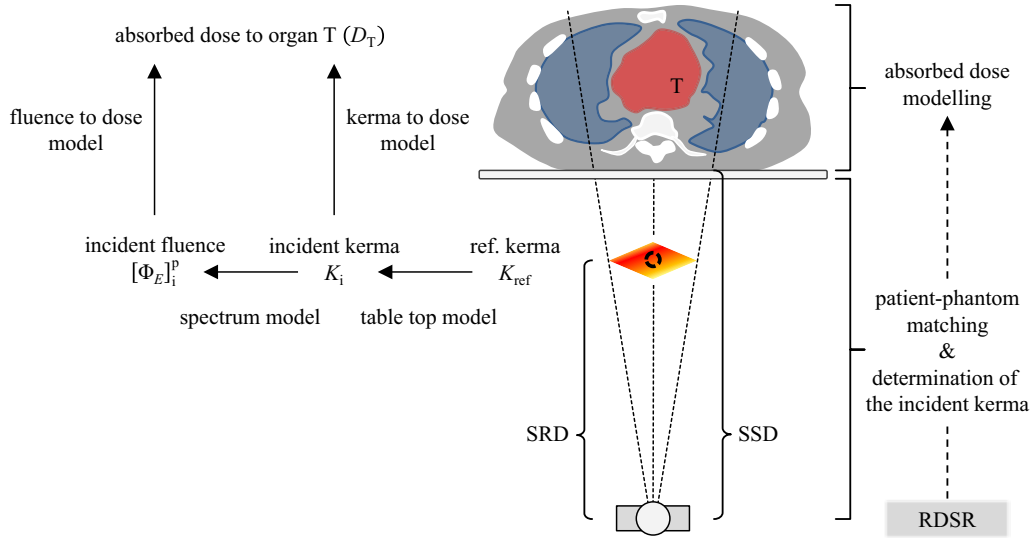


Figure 1. Illustration of the general framework for the determination of absorbed (or equivalent) dose to internal organs and to the skin from the reference air kerma free-in-air at the central axis of the x-ray beam. The calculation workflow is shown in terms of the kerma free-in-air, K , and the primary (p) photon fluence differential in energy, $[\Phi_E]^p$. SRD and SSD is the source-to-reference and source-to-skin distance, respectively. Also shown is the information process for utilizing RDSR in the calculation workflow (hatched arrow).

extraction of RDSR is the topic of section 2.1.1, and the details of the framework are presented in the subsequent sections 2.1.2 and 2.1.3.

2.1.1. Extraction of DICOM RDSR objects In accordance with IEC 60601-2-43 2nd edition (IEC, 2010) RDSR is now required to be supported on new XA systems in order to facilitate non-proprietary access to examination data. The data contained in the RDSR is structured as a nested set (hierarchical tree) with well defined templates. For dosimetry, the main template is the Irradiation Event X-ray Data container (TID 10003), which contains dose-related data for the irradiation events of a performed procedure. An irradiation event is defined as a single use of radiation during a continuous length of time as part of the examination (NEMA, 2015). Therefore, an irradiation event could constitute a single fluoroscopy run, i.e. radioscopy, a set of stationary acquisitions, i.e. radiography, or a single rotational acquisition, e.g. c-arm cone beam CT (CBCT) or 3D rotational angiography (3DRA). Depending on the complexity of the XA examination, the RDSR may contain dose-related data for hundreds of individual irradiation events.

In order to extract the data contained in the RDSR, the XA system must be configured to transfer RDSR objects to a DICOM server where a parser (e.g. DICOM reader) is applied. In this work, a DICOM server was installed locally using *Conquest DICOM software* (Netherlands Cancer Institute, Amsterdam, the Netherlands). The clinical XA systems at Karolinska University Hospital, Stockholm, Sweden, were configured to automatically transfer the associated RDSR objects to the DICOM server

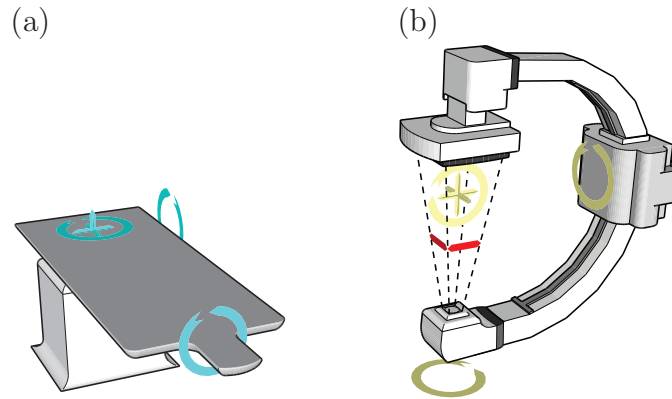


Figure 2. Schematic illustration of an XA system and the geometrical parameters that describe (a) the position of the patient table top, and (b) the geometry of the x-ray beam. The table top movement and tilting axes are shown in blue. The c-arm movement and rotation axes about the isocenter are shown in yellow. The collimated height and width of the x-ray beam is shown in red.

at the end of each procedure. A parser was developed using the *Pixelmed Java DICOM Toolkit* (Pixelmed Publishing, Bangor, PA, USA) to extract the information contained in the received RDSR objects, which are then sent to an open source database (MySQL, Oracle Corporation, Redwood City, CA, USA). The database also includes data on patient height and weight extracted from the hospital information system (HIS). Information that can be used to identify the patient, e.g. name and personal identification number, are anonymised to preserve healthcare information privacy.

2.1.2. Determination of the incident kerma The radiation exposure incident on the patient surface can be modelled in its entirety by taking the physical context of each irradiation event into account. The parameters necessary to describe the physical context are:

- (a) Geometrical parameters that describe the position of the patient table top, illustrated in figure 2(a).
- (b) Geometrical parameters that describe the size, direction and position of the x-ray beam, illustrated in figure 2(b).
- (c) Parameters that characterise the x-ray beam quality and photon fluence.

The RDSR dose-related data that can be used to describe the physical context are summarised in table 1.

To determine the incident kerma, the fluence of the emitted x-ray beam needs to be known for each separate irradiation event. For that purpose, the tube current-exposure time product (mAs), which is contained in the RDSR, can be used together with x-ray tube and beam quality specific conversion factors to account for the particular tube output. Considering that such factors are usually not readily available, it is generally more convenient to use the reference kerma free-in-air, K_{ref} , which is in accordance with

current standards included in the RDSR as the air kerma free-in-air, $K_{\text{air,ref}}$. The use of air kerma for the determination of dosimetry quantities in diagnostic radiology is well established and consistent with ICRU74 (ICRU, 2006) and the IAEA TRS-457 code of practice (Alm-Carlsson et al., 2009). Note that if $K_{\text{air,ref}}$ is used, it is crucial that the accuracy of the reported value is regularly tested as part of a clinical quality assurance program.

The $K_{\text{air,ref}}$ can be transferred into incident air kerma at the patient entrance surface as

$$K_{\text{air,i}} = K_{\text{air,ref}} f_{\text{table}} (\text{SRD}/\text{SSD})^2, \quad (1)$$

where the table transmission factor, f_{table} , accounts for the attenuation of the patient table, SRD is the source-to-reference distance and SSD is the source-to-surface distance. The table transmission has traditionally been determined experimentally for normally incident x-ray beams, ignoring the greater attenuation of an obliquely incident beam. Therefore, an analytical approach is proposed,

$$f_{\text{table}} = \frac{\int_0^{E_{\text{max}}} E [\Phi_E]^p [\mu_{\text{en}}(E)/\rho]_{\text{air}} F(E, \theta, \varphi) dE}{\int_0^{E_{\text{max}}} E [\Phi_E]^p [\mu_{\text{en}}(E)/\rho]_{\text{air}} dE}, \quad (2)$$

where $[\mu_{\text{en}}(E)/\rho]_{\text{air}}$ is the photon mass energy-absorption coefficient in air for photons of energy E , and $[\Phi_E]^p$ is the primary (p) photon fluence differential in energy normalized to unit fluence, i.e. the normalized emitted photon spectrum free-in-air. This spectrum can be analytically calculated using a model such as Birch and Marshall (1979) or Poludniowski (2007). Further, $F(E, \theta, \varphi)$ is the transmission of the table top and pad calculated for monoenergetic photons incident onto the table plane at c-arm RAO (right anterior oblique) to LAO (left anterior oblique) rotation angle, θ , and c-arm CAU (caudal) to CRA (cranial) rotation angle, φ ,

$$F(E, \theta, \varphi) = \exp \left(- \sum_i [\mu(E)/\rho]_i (\rho\ell)_i \sqrt{\tan^2\theta + \tan^2\varphi + 1} \right), \quad (3)$$

where $[\mu(E)/\rho]_i$ is the photon mass attenuation coefficient for material i and $(\rho\ell)_i$ is the mass thickness of material i . The mass thickness of the table and pad is not available from the RDSR and therefore has to be considered separately. The mass thickness can be determined in terms of carbon and water equivalent thickness from air kerma transmission measurements for clinical emitted beam qualities, or it can be determined based on information provided by the manufacturer.

Although the SSD in equation (1) is not available from the RDSR, it can be approximated based on the assumption that the patient entrance surface coincides with the surface of a phantom model whose size and shape has been matched to that of the patient. Patient-phantom matching and how it is dealt with within the scope of the proposed framework is the subject of the following section.

2.1.3. Patient-phantom matching In order to convert the incident kerma to absorbed organ dose, it is imperative that the geometrical relation between the projected x-ray

beam and the patient's anatomy is accurately reconstructed. This is the purpose of patient-phantom matching, for which the essential parameters are:

- (a) Parameters that describe the size and shape of the patient's body.
- (b) Parameters that describe the position and orientation of the patient on the table top.

The RDSR dose-related data that are relevant for patient-phantom matching are summarised in table 1.

Based on the parameters that describe the size and shape of the patient's body, a matching phantom model can be selected. There are various models representing patients of different ages, genders, heights and weights available (Xu, 2014), any of which can be used within the framework. The benefits and limitations of different types of phantom models for fluoroscopy guided interventions have been investigated elsewhere (Johnson et al., 2011*b*).

With a suitable phantom model selected the next step is the geometrical alignment of the phantom with the projected x-ray beam, i.e. reconstruction of the patient-beam alignment. This can be achieved by matching the orientation and position of the phantom to the patient's position and orientation on the table top. Unfortunately, this is not trivial, as the position of the patient is generally unknown. The few applications that have been developed for estimation of organ (skin) dose based on RDSR data (Khodadadegan et al., 2011; Johnson et al., 2011*a*) use a standard patient position. The standard position approach (henceforth referred to as the head-centric approach, HC) is based on the assumption that the patient's head is placed centrally on the table top at a predetermined distance from the head end of the table. Such an approach relies on that the patient position is consistently reproducible and that the distance between the patient's head and organs away from the head, such as the target organ (e.g. the heart for cardiovascular procedures), are correctly imitated by the phantom model. These assumptions may introduce substantial errors in the determination of absorbed organ dose as the dose may be calculated to other organs than the ones actually irradiated. Hence, to improve the accuracy in dose estimations, a patient-specific method is introduced as part of the framework: the target-centric approach (TC). The proposed approach is based on locating the position (midpoint) of the patient's target organ in relation to the head end of the table, and then using that as origin for the reconstruction of the patient-beam alignment. By using the location of the target organ as origin instead of the head, the accuracy of the alignment is expected to be improved for organs proximal to the target organ region, i.e. for the primarily irradiated organs. The target-centric approach locates the target organ by taking advantage of the fact that although various irradiation geometries are used throughout a procedure, most of the irradiation time is dedicated to visualizing the region of the target organ. Therefore, the position of the target organ can be estimated as the median position of the isocenter

relative to the head end of the table,

$$\mathbf{r}_{\text{target}}^{\text{TC}} = \sum_{i \in \{x, y, z\}} \text{median}(\{\mathbf{r}_{\text{iso}}(t) \cdot \mathbf{e}_i \mid t \in \mathcal{X}\}) \mathbf{e}_i, \quad (4)$$

where $\mathbf{r}_{\text{iso}}(t) = (x, y, z)$ is the x-ray beam isocenter position relative to the head end of the table at irradiation time t , and $\{\mathbf{e}_x, \mathbf{e}_y, \mathbf{e}_z\}$ are unit vectors that form the standard basis. The set \mathcal{X} excludes time periods when the irradiation of the patient is presumably not aimed at the visualization of the target region. For instance, this may for certain types of neurovascular procedures be the exclusion of time periods when the x-ray beam isocenter is located outside of the limitations imposed by a head fixation apparatus. The purpose of defining such limits is to improve the accuracy in estimated target organ position. Note that the median is used instead of the mean in the above equation for the same reason — that is, to improve the accuracy in estimated target organ position by excluding time periods when the irradiation geometry is not aimed at the visualization of the target organ, i.e. by reducing the impact of the outlying $\mathbf{r}_{\text{iso}}(t)$. With the target organ position located, the position of the isocenter in relation to the patient’s anatomy at irradiation time t is reconstructed as $\mathbf{r}_{\text{iso}}(t) - \mathbf{r}_{\text{target}}^{\text{TC}}$. Details associated with implementation of the target-centric approach using data contained in the RDSR are given in Appendix A.

In order to evaluate the difference in accuracy of the target- and head-centric approach, a ground truth target organ position was determined using clinical DICOM images. The target organ was located in the DICOM images corresponding to posterior-anterior (PA) and lateral projections (LAT) for 50 neurovascular, 50 adult and 50 paediatric cardiovascular procedures. The position of the target organ was determined relative to the head end of the table using the isocenter position, table top head end position, image pixel size and distance measurements provided in the DICOM header. The position was identified as the geometrical center of the brain for neurovascular procedures and the midpoint of the heart for cardiovascular procedures (aortic valve used as landmark).

Table 1. Parameters that can be used to describe the physical context of an irradiation event (a)–(c) and patient descriptors (d)–(e), related to DICOM RDSR objects of NEMA (2015). The requirement types of the RDSR data in the scope of a vendor implementation are: M, mandatory — shall be present; MC, mandatory conditional — shall be present if certain conditions are satisfied; U, user option — may be present; UC, user option conditional — may be present if certain conditions are satisfied.

Parameter	(Context Group ID; CID) RDSR Concept Name	Type	Comment
(a) Patient Table Top Position:			
Position (x)	(113751) Table Longitudinal Position	U	Along the table width direction
Position (y)	(113753) Table Height Position	U	Along the table height direction
Position (z)	(113752) Table Lateral Position	U	Along the table length direction
Head tilt	(113754) Table Head Tilt Angle	U	
Cradle tilt	(113756) Table Cradle Tilt Angle	U	
Horizontal rotation	(113755) Table Horizontal Rotation Angle	U	
(b) X-ray Beam Geometry:			
Isocenter position (x,y,z) ^a			<i>Not supported by DICOM RDSR</i>
Source-to-isocenter distance (SID)	(113748) Distance Source to Isocenter	U	
C-arm RAO–LAO ^b rotation (θ)	(112011) Positioner Primary Angle	UC	
C-arm CAU–CRA ^c rotation (φ)	(112012) Positioner Secondary Angle	UC	
Collimated beam size	(113788,113789) Collimated Field Height, Width	U	
(c) Beam Quality and Fluence:			
K_{ref}	(111636) Entrance Exposure ^d at RP	MC	$K_{\text{air,ref}}$ according to current standards ^f
Source-to-reference distance (SRD)	(113737) Distance Source to Reference Point	U	
mAs	(113736) Exposure ^e	MC	Mean tube current-exposure time product
Tube kilovoltage (kV)	(113733) KVP	M	Measured/recorded mean value or per pulse
Filter type	(113772) X-Ray Filter Type	U	
Filter material	(113757) X-Ray Filter Material	U	
Filter thickness	(113758) X-Ray Filter Thickness Minimum	U	Inherent filtration not included
Table material and geometry			<i>Not supported by DICOM RDSR</i>
(d) Patient Body Size and Shape:			
Height and weight		U	Provided in RDSR as a patient descriptor
Sex		U	Provided in RDSR as a patient descriptor
Age		U	Provided in RDSR as a patient descriptor
(e) Patient Position and Orientation:			
Position (x,y,z)			<i>Not supported by DICOM RDSR</i>
Source-to-surface distance (SSD)			<i>Not supported by DICOM RDSR</i>
Patient table top relationship	(113745) Patient Table Relationship	U	E.g. headfirst or feet-first
Patient orientation	(113744) Patient Orientation Modifier	U	E.g. prone or supine

^aThe isocenter position is redundant if the table top position is defined relative to the isocenter (as was the case for the RDSR used in this work).

^bX-ray image detector rotation angle from RAO (right anterior oblique) to LAO (left anterior oblique) direction with origin perpendicular to the patient’s chest.

^cX-ray image detector rotation angle from CAU (caudal) to CRA (cranial) direction with origin perpendicular to the patient’s chest.

^{d,e}Note that the term ‘Exposure’ is in the DICOM RDSR incorrectly used to refer to the physical quantity of ^dkerma and ^emAs.

^fDefined as the $K_{\text{air,ref}}$ at the patient entrance reference point (PERP) located on the central axis 15 cm from the isocenter towards the x-ray tube (IEC, 2010).

2.2. Prototype implementation of the framework

To demonstrate the utility of the framework for organ dose estimation in routine clinical practice, a prototype implementation of the framework was constructed in *MATLAB* (The Mathworks Inc., Nattick, MA, USA). In order to take into account radiation transport in the patient, the framework was connected to the commercial MC program *PCXMC* (STUK, Helsinki, Finland) (Servomaa and Tapiovaara, 1998). Although there are other more sophisticated MC codes available, they are generally substantially slower due to more complex physics and phantom modelling. Considering that an XA procedure may consist of hundreds of separate irradiation events and that several thousand XA procedures a year may be performed at a large hospital, timely and efficient dose calculations are essential. *PCXMC* calculates absorbed (equivalent) organ doses and effective doses by first converting $K_{\text{air},i}$ to incident spectrum, $[\Phi_E]_i^p$, using the spectrum model by Birch and Marshall (1979), and then simulating 2 million histories per 10 keV photon energy bin. A script was created that automatically generates an input file, initiates *PCXMC* with the command line, and extracts data from the generated output file. The script manages each irradiation event in sequence without the need for any user interference.

The prototype implementation of the framework is demonstrated for 50 neurovascular procedures (30 female and 20 male patients, 11–76 years old), 50 adult cardiovascular procedures (16 female and 34 male patients, 32–95 years old), and 50 paediatric cardiovascular procedures (34 female and 16 male patients, newborn–16 years old). The procedures were performed in interventional laboratories equipped with AlluraClarity XA systems (Philips Healthcare, Best, the Netherlands). The neurovascular laboratory was equipped with an FD20/20 (large detector) biplanar system, the adult cardiovascular laboratory with an FD10 (small detector) monoplanar system, and the paediatric cardiovascular laboratory with an FD10/10 (small detector) biplanar system.

2.2.1. Determination of the incident kerma

The framework was implemented according to section 2.1.2 to determine the incident kerma for each irradiation event of an XA procedure. The $K_{\text{air},i}$ was calculated using equation (1), with $K_{\text{air,ref}}$ and SRD values extracted from RDSR. The SSD was approximated by analytical ray tracing to find the distance from the x-ray source to the surface of the phantom model whose size and shape has been scaled to emulate that of the patient (patient-phantom matching is the subject of the following section 2.2.2). For the table transmission, RDSR data describing the position and angulation of the projected x-ray beam were used to determine if the x-ray beam intersects the table, and f_{table} was calculated using equation (2). The $[\mu_{\text{en}}(E)/\rho]_{\text{air}}$ and $[\mu(E)/\rho]$ values were taken from the NIST database (Hubbell and Seltzer, 2004), and $[\Phi_E]_{\text{ref}}^p$ was calculated by the analytical method of Poludniowski (2007) with data generated by Poludniowski and Evans (2007) and with RDSR data specifying the emitted beam quality. As the inherent filtration of the x-

ray tube and tube housing is not included in the RDSR, it was taken into account using the aluminium equivalent thickness measured with a multi-purpose detector and a Barracuda electrometer (RTI Electronics AB, Sweden). Further, the mass thickness of the AlluraClarity table, in terms of carbon and water, was determined from air kerma transmission measurements carried out for clinically relevant emitted beam qualities using an R100B dose probe attached to the Barracuda electrometer. A wide beam geometry was used so as not to underestimate the contribution from photons forward scattered from the patient table in the calculation of transmitted air kerma. Completely ignoring the photons scattered from the table would bias the absorbed organ doses to be systematically underestimated.

For rotational acquisition irradiation events, the absorbed organ dose should ideally be determined as the sum of the absorbed dose from each individual projection x-ray image acquired during that event. As the RDSR of the XA systems used in this work do not provide information about individual projection images, the mean tube kilovoltage and accumulated $K_{\text{air,ref}}$ for the whole event were used to approximate the x-ray beam quality and photon fluence. Based on the approximation that the $K_{\text{air,ref}}$ is evenly distributed amongst the different projection images, rotational irradiations can be modelled as a set of beam projections rotated around the isocentre, with $K_{\text{air},i}$ calculated separately for each projection. The circular trajectory of single axis rotational irradiations were modelled as equidistantly spaced projections, 3° apart in rotation angle. The curved trajectory of dual axis rotations were modelled using a template outlining the c-arm movement, which was constructed using information available in DICOM header tags describing the incremental change in rotation angle.

2.2.2. Patient-phantom matching *PCXMC* uses the slightly modified and updated stylized hermaphrodite phantom models of Cristy and Eckerman (1987) (newborn, 1, 5, 10, 15 and 30 years old). Patient descriptors regarding the age, height and weight of the patient were used to scale the size, mass and position of the phantom's organs according to ICRU (2005). It should be acknowledged that these phantoms are of limited realism compared to modern voxelized and hybrid phantoms. However, using these simplistic mathematical phantoms with the *PCXMC* software allows for highly efficient dose simulations, which is currently a necessity for dose estimations for large patient populations, or for routine dose calculations at a large clinic.

For accurate dose estimations, it is essential that the geometrical parameters found in the RDSR are correctly translated to the phantom coordinate system used in *PCXMC*. For that purpose the target- or the head-centric approach, described as part of the framework (section 2.1.3), was used to match the position of the target organ or the head of the patient to that of the phantom, respectively. For the head-centric approach, the standard position of the patient's head relative to the head end of the table was set as the position that minimizes the error in target organ position compared to its ground-truth position located in clinical DICOM images (i.e. the best-case standard position was assumed). For the target-centric approach, the target organ was for neurovascular

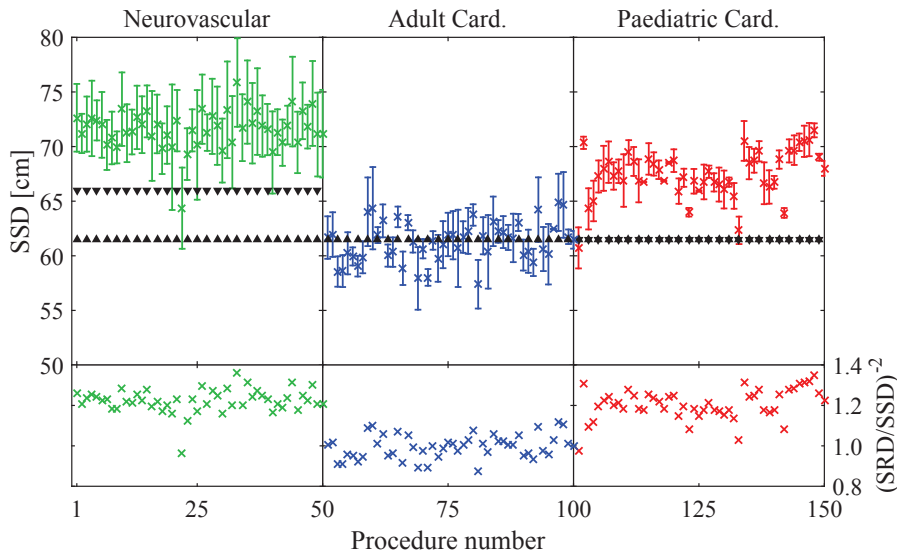


Figure 3. The upper panels show the mean source-to-surface distance (SSD) calculated for different clinical procedures. Also shown is the source-to-reference distance (SRD) for the frontal (\blacktriangle) and lateral (\blacktriangledown) acquisition plane. The lower panels show squared ratios of SSD to SRD, i.e. the inverse square law. The presented values are averaged over the various irradiation events of each procedure, weighted by their respective $K_{\text{air,ref}}$. The uncertainty bars correspond to one standard deviation.

procedures specified to be the brain, and for cardiovascular procedures to be the heart.

3. Results and discussion

3.1. Determination of the incident kerma

To determine the incident kerma, the source-to-surface distance (SSD) needs to be determined and the attenuation of the patient table needs to be accounted for. The mean SSD calculated for the procedures considered in this work using mathematical phantom models whose size and shape has been matched to that of the individual patients, is shown in the upper panel of figure 3. The values are averaged over the irradiation events of each procedure, weighted by their respective $K_{\text{air,ref}}$. For comparison, the SRD for each acquisition plane of the different XA systems is also shown. Although the patient entrance reference point (PERP) is defined in such a way as to coincide approximately with the patient entrance surface, the results indicate that it does so only for adult cardiovascular procedures. For neurovascular and paediatric cardiovascular procedures, the mean SSD is substantially greater than the SRD, being 71.6 ± 3.0 and 67.6 ± 1.1 cm, respectively, compared to 61.3 ± 1.7 cm for the adult cardiovascular procedures and an SRD of 61.5 cm for the frontal acquisition plane. Thus, approximating the geometry- and patient-specific SSD as the SRD may overestimate the $K_{\text{air,i}}$ (equation (1)) by up to 40%, as is shown in the lower panel of figure 3.

Regarding the attenuation of the patient table top and pad, measured and

Table 2. Air kerma transmission factors for the AlluraClarity patient table measured for a PA projection, and calculated using equation (2) with an angle of incidence of ($\theta = 0, \varphi = 0$), a mass thickness of 2.5 mm carbon (2.0 g/cm^3) and 0.5 mm water (epoxy resin) for the table top, and a mass thickness of 4 mm water (PU foam) for the pad. The measured air kerma transmission factors with and without the pad have an estimated combined standard uncertainty of about 1% and 2%, respectively.

kV	Inherent filtration (mm Al)	Added filtration (mm Cu)	HVL ₁ (mm Al)	f_{table}		$f_{\text{table+pad}}$	
				Measured	Calculated	Measured	Calculated
50	3.5	0.0	2.38	0.83	0.85	0.71	0.72
80	3.5	0.0	3.75	0.86	0.87	0.76	0.76
60	4.5	0.4	5.40	0.90	0.89	0.81	0.81
70	4.5	0.9	7.74	0.91	0.90	0.84	0.83
100	4.5	0.9	10.2	0.92	0.91	0.84	0.84

calculated air kerma transmission factors for the AlluraClarity patient table are listed in table 2, together with values calculated using equation (2). The calculated factors are generally within the measurement uncertainty, having a maximum relative deviation of 2.5%. As expected, the attenuation is greater for lower tube potentials and thinner filtrations due to the relatively greater amount of low energy photons in the x-ray beam. The results indicate that the incident $K_{\text{air},i}$ (equation (1)) may be overestimated by more than 15% if the table top attenuation is not included in the calculations. The results also show the importance of taking into account the combined attenuation of the table top and pad, as that may result in an attenuation of up to 30%.

3.2. Target organ localisation

Figure 4 shows target organ positions located in DICOM images corresponding to PA (a) and LAT (b) projections for the clinical procedures considered in this work. LAT projections were not available for the adult cardiovascular procedures as they were performed in an interventional laboratory equipped with a monoplanar (frontal plane) XA system. In general, there was a wide spread in target organ position, especially in the longitudinal direction. The one standard deviation in longitudinal direction being 3.0, 6.0 and 9.7 cm, and the range being 13.2, 27.6 and 49.1 cm for neurovascular, adult and paediatric cardiovascular procedures, respectively. The head fixation apparatus used for neurovascular procedures limits movement of the head in the lateral direction, which explains the narrow spread of the midpoint of the brain in that direction.

A prerequisite for using a standard geometry to reconstruct the patient-beam alignment (i.e. the head centric approach), is that the positioning of the patient on the table can be consistently reproduced. This means that the observed spread in target organ position should be mainly attributed to the variation in patient size and not be due to a large variation in the positioning of the patient on the table. In order to evaluate to what extent the spread in target organ position can be attributed to the variation in patient size, the linear correlation between the target organ position and patient age, BMI, weight and height, was analysed. Nearly all of these correlations were

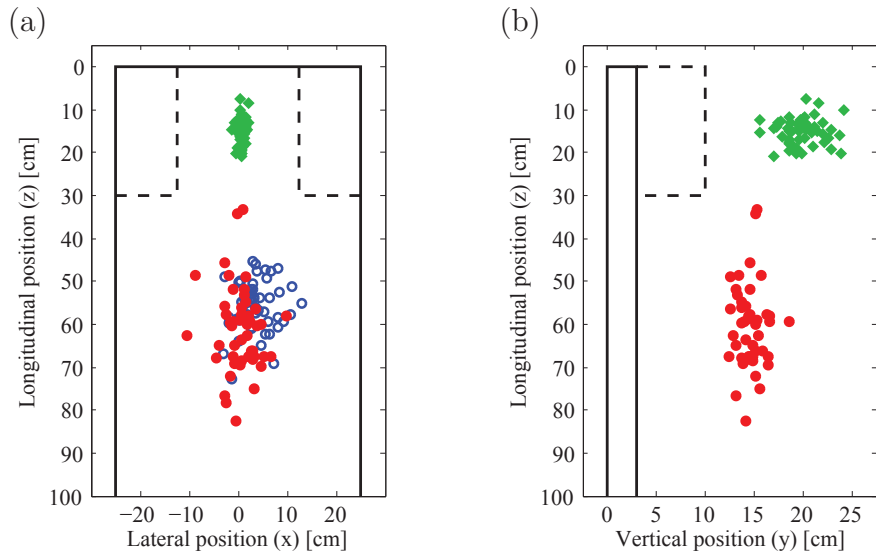


Figure 4. Target organ positions relative to the head end of the table localised in the clinical DICOM images of 50 neurovascular (\blacklozenge), adult (\circ) and paediatric (\bullet) cardiovascular procedures. The target organ positions are projected onto (a) the coronal plane and (b) the sagittal plane of the patient. The contours of the cardiovascular table top (line) and the neurovascular table top and head fixation apparatus (dashed line) are outlined for illustrative purposes.

absent and the rest indicated only a weak trend. This argues that the main cause for the large spread in target organ position is the variation in the positioning of the patient on the table top. The conclusion is also consistent with the observed clinical routine practice for the positioning of the patient, especially for acute clinical procedures for which time is of the essence.

3.3. Reconstruction of the patient-beam alignment

To compare the accuracy of the proposed target-centric approach with that of the head-centric approach, the target organ positions estimated by the two methods were compared to the position located in clinical DICOM images, i.e. the ground truth. Recalling that the head-centric approach gives the position of the patient's head, the distance from the patient's head to the midpoint of the target organ needs to be determined to locate the target organ position using this approach. As the actual distance is unknown, it was estimated for each patient to be the corresponding distance in the age appropriate phantom model of Cristy and Eckerman (1987), whose dimensions have been scaled to match the height and weight of the patient according to ICRU (2005). Although the estimated distance in the phantom may be slightly different for other types of phantom models, this difference is expected to be small compared to the difference to the actual distance in the patient. Therefore, the presented results are relevant for any type of phantom model, as they reflect the limitations associated with the head-centric approach, more so than the limitations of the used phantom model.

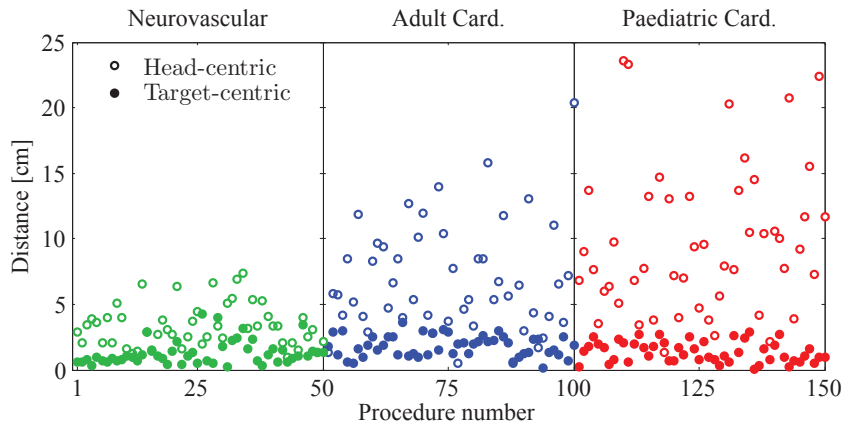


Figure 5. Distance from the target organ position located in clinical DICOM images to the position estimated by the indicated approach for the reconstruction of the patient-beam alignment.

As shown in figure 5, the target-centric approach was overall distinctly more accurate and precise than the head-centric approach, locating the position of the target organ to within 5 cm compared to 25 cm for all procedures considered in this work. Even though the target-centric approach was notably more accurate for the neurovascular procedures, both approaches were fairly accurate, having a mean deviation of 1.3 and 3.4 cm, and a maximum deviation of 4.3 and 7.4, respectively, for the target- and head-centric approach. This was expected as the head was the target organ region for the neurovascular procedures, and a head fixation apparatus was used for these procedures to ensure suitable placement of the patients' heads. For the adult and paediatric cardiovascular procedures, the target-centric approach was substantially more accurate in locating the midpoint of the heart, having a mean deviation of 1.8 and 1.4 cm compared to 6.9 and 9.7 cm, respectively. The maximum deviation was limited to 3.6 and 2.9 cm using the target-centric approach compared to 20.4 and 23.5 cm using the head-centric approach. These results indicate that the proposed target-centric approach can provide a major improvement over the head-centric approach for reconstruction of the patient-beam alignment in the target organ region, i.e. the primarily irradiated body region.

The difference in accuracy of calculated absorbed organ doses when using the target- or head-centric approach was investigated by using the prototype implementation of the framework to calculate the doses to the study population. The resulting doses were compared with absorbed organ doses calculated using clinical DICOM images as the ground truth for the reconstruction of the patient-beam alignment. The results are presented in table 3, where the percent difference in population dose, i.e. the cumulative dose for the study population, and the maximum absolute difference in dose to relevant organs and effective doses are tabulated. The target-centric approach is shown to provide considerably more accurate dose estimates compared to the head-centric approach, having a percent difference in population dose mostly within 5%. The head-centric

Table 3. Difference in absorbed organ (mGy) and effective (mSv; ICRP 103 (ICRP, 2007)) doses calculated for the study population (represented by the phantom models of Cristy and Eckerman (1987)) using the target- and head-centric approach compared to doses calculated using clinical DICOM images as the ground truth for the reconstruction of the patient-beam alignment. Tabulated is the percent difference (PD) in population dose and the maximum absolute difference (Max) in procedural dose. The Max dose difference normalized by the corresponding (ground truth) absorbed dose to the target organ is also shown in brackets ($/D_{\text{target}}$).

	Target-centric		Head-centric	
	PD [%]	Max [mGy] ($/D_{\text{target}}$)	PD [%]	Max [mGy] ($/D_{\text{target}}$)
Neurovascular				
Active bone marrow	-1.4	0.6 (0.01)	-4.8	2.3 (0.03)
Brain	3.7	12.9 (0.16)	-5.8	32.3 (0.59)
Thyroid	-4.4	2.7 (0.09)	7.9	13.3 (0.24)
Average dose in body	-1.4	0.6 (0.01)	-3.9	2.1 (0.03)
Effective dose	-4.6	0.6 (—)	-3.0	2.2 (—)
Adult Cardiovascular				
Active bone marrow	0.6	4.1 (0.06)	-4.1	7.0 (0.15)
Breasts	3.8	1.2 (0.02)	25.1	6.8 (0.15)
Heart	-4.6	8.0 (0.09)	-34.5	41.5 (0.49)
Liver	-3.8	6.7 (0.19)	-35.2	16.2 (0.19)
Lungs	-0.8	17.5 (0.25)	-12.1	31.6 (0.45)
Oesophagus	1.7	10.8 (0.15)	-17.3	31.2 (0.67)
Stomach	-13.7	1.6 (0.04)	74.6	20.5 (0.29)
Average dose in body	0.0	0.4 (0.01)	-2.2	1.9 (0.04)
Effective dose	-1.4	1.0 (—)	-2.1	2.7 (—)
Paediatric Cardiovascular				
Active bone marrow	-3.3	0.8 (0.04)	-7.4	4.3 (0.23)
Breasts (female)	14.0	10.6 (0.68)	-83.0	22.8 (0.97)
Heart	2.9	2.5 (0.17)	-63.7	19.0 (0.81)
Liver	-3.9	3.4 (0.18)	22.1	24.5 (0.90)
Lungs	-4.1	3.4 (0.18)	-55.4	23.2 (1.23)
Oesophagus	-1.1	3.4 (0.14)	-43.1	19.4 (1.02)
Stomach	3.5	1.2 (0.06)	16.5	7.5 (0.40)
Average dose in body	-2.7	1.0 (0.05)	-9.4	5.5 (0.29)
Effective dose	1.2	1.1 (—)	-33.3	8.5 (—)

approach, on the contrary, is shown to provide a percent difference in excess of 30% for several organs, spanning to as much as 80%. Using the target-centric approach, the percent difference exceeds 5% only for dose to the stomach and breast tissue for adult and paediatric cardiovascular procedures, respectively. However, it is important to note that the dose to the stomach is generally relatively low for cardiovascular procedures, and the maximum absolute difference is therefore limited to about 2 mGy, or about 5% of the absorbed dose to the target organ. Also, the dose to the breast tissue for paediatric patients is difficult to estimate considering that the volume of the tissue is small and highly localised (less than 2.5 cm³ for phantom models corresponding to patients younger than 15 years). Hence, even a small mismatch between the phantom model and the patient anatomy may result in a large deviation, making any estimate of dose to breast tissue for paediatric patients inherently associated with a large model uncertainty. The results also suggest that the target-centric approach is markedly more robust, as the maximum absolute difference is substantially smaller for all organs. It should be noted

that the numerical values of table 3 are representative of the phantom models used in this work, and are expected to be to some extent different for other types of phantom models. However, the considerable differences in both the accuracy and precision of the estimated absorbed organ doses demonstrated here, clearly indicate that the proposed target-centric approach should be a major improvement over previous methods, for any type of phantom model. This is also substantiated by the excellent agreement of the target organ position estimated using the target-centric approach compared with its ground truth position (shown in figure 5).

3.4. Absorbed organ dose estimation

To demonstrate the utility of the framework for organ dose estimation in routine clinical practice, absorbed organ and effective doses were estimated for the study population using the developed prototype implementation of the framework described in section 2.2. The prototype simulates the radiation transport in the patient in a timely and efficient manner; the calculation time was 10–30 minutes per XA procedure, depending on the number of irradiation events, using two 2.3 Ghz Intel Xeon CPUs. The estimated doses for clinical XA procedures are presented in Table 4. For neurovascular procedures, the stationary acquisitions (radiography) contribute the most to the absorbed dose, which is primarily due to the high image quality required to visualize the fine vasculature of the brain. For adult cardiovascular procedures the contribution to the absorbed dose is evenly distributed between fluoroscopy (radioscopy) and stationary acquisitions, while the dose from rotational irradiations is minimal. For paediatric cardiovascular procedures the majority of the contribution to the absorbed dose comes from fluoroscopy, while the contribution from radiography is minimal, which is likely due to an effort to avoid unnecessary high radiation exposure. The average absorbed organ dose per $K_{\text{air,ref}}$ is for paediatric patients more than five times greater than for adult patients. This is mainly due to the x-ray beam covering a greater part of the patient body and also due to the patients having less adipose and muscle tissue attenuating the incident beam.

Comparing the absorbed organ doses calculated in this work with those found in the literature is difficult, as the dose depends greatly on the complexity of procedure, irradiation geometry, system settings and patient population. Furthermore, calculation of absorbed organ doses in such detail as presented in this work has traditionally not been possible for XA procedures. Any comparison of absorbed organ dose would thus inherently be biased due to the large difference in the sophistication of dose estimation. Therefore, in order to compare the results of this work with those found in the literature, effective doses calculated as weighted summations of absorbed organ doses, normalized to accumulated dose indices of air kerma-area product, P_{KA} , were used instead. The rationale for this is that such a normalized integral dose quantity should be less sensitive to difference in complexity of procedure and difference in sophistication of the dose calculation introduced, for instance, by the reconstruction of the patient-beam alignment. Table 5 shows a summary of relevant P_{KA} to effective dose conversion

Table 4. Mean absorbed organ doses (mGy) and effective doses (mSv; ICRP 103 (ICRP, 2007)) calculated per procedure for the study population using the target-centric approach for the reconstruction of the patient-beam alignment. The tabulated mean doses for the rotational acquisition irradiation events are per rotational event instead of per procedure. The values are presented along with the standard deviation of the mean, σ . The mean total dose normalized by the cumulative reference point air kerma is also shown in brackets ($/K_{\text{air,ref}}$).

	Fluoroscopy		Stationary acquisition		Rotational acquisition		Total			
	Mean	σ	Mean	σ	Mean	σ	Mean ($/K_{\text{air,ref}}$)	σ	Max	
Neurovascular										
Active bone marrow	1.5	0.2	3.0	0.3	0.4	0.1	4.9 (0.02)	0.5	13.2	
Brain	4.3	0.4	27.9	3.3	4.8	0.4	38.5 (0.18)	3.6	116.2	
Thyroid	4.7	0.7	3.9	0.5	0.1	0.0	8.7 (0.04)	1.1	35.7	
Effective dose	0.9	0.1	1.5	0.2	0.2	0.0	2.6 (0.01)	0.3	8.6	
Adult Cardiovascular										
Active bone marrow	4.3	0.6	3.7	0.4	0.5	0.1	8.1 (0.02)	0.8	25.1	
Breasts	1.4	0.2	1.1	0.1	0.1	0.0	2.5 (0.01)	0.3	10.0	
Heart	10.4	1.5	9.9	1.2	1.3	0.3	20.5 (0.04)	2.2	76.4	
Liver	2.6	0.4	2.6	0.3	0.4	0.2	5.2 (0.01)	0.5	18.0	
Lungs	9.8	1.3	9.8	1.1	1.2	0.2	19.7 (0.04)	2.0	78.0	
Oesophagus	9.7	1.4	7.8	0.8	1.0	0.3	17.6 (0.04)	1.8	52.9	
Stomach	1.1	0.2	1.0	0.1	0.2	0.1	2.1 (0.00)	0.2	9.9	
Effective dose	3.0	0.4	2.7	0.3	0.4	0.1	5.7 (0.01)	0.5	18.7	
Paediatric Cardiovascular										
Active bone marrow	1.0	0.2	0.1	0.0	—	—	1.2 (0.04)	0.2	6.6	
Breasts	4.1	0.6	0.8	0.2	—	—	5.0 (0.18)	0.7	20.9	
Heart	5.1	0.8	1.0	0.2	—	—	6.1 (0.22)	0.9	27.2	
Liver	2.1	0.4	0.4	0.1	—	—	2.5 (0.09)	0.4	16.2	
Lungs	5.8	0.9	1.0	0.2	—	—	6.9 (0.25)	1.0	29.3	
Oesophagus	4.1	0.6	0.7	0.1	—	—	4.8 (0.17)	0.7	18.4	
Stomach	1.1	0.2	0.2	0.0	—	—	1.3 (0.05)	0.2	6.4	
Effective dose	2.0	0.3	0.3	0.1	—	—	2.3 (0.08)	0.3	8.8	

Table 5. Mean P_{KA} to effective dose conversion coefficients (C_E) in units of mSv/mGycm²

Procedure	Reference	C_E
Neurovascular	Manninen et al. (2012)	0.06–0.07
	NCRP (2009)	0.09
	This work	0.08
Adult Cardiovascular	Compagnone et al. (2011)	0.11–0.20
	IAEA (2009)	0.18
	NCRP (2009)	0.12–0.28
	This work	0.22
Paediatric Cardiovascular	Karambatsakidou et al. (2009)	(3.7, 1.9, 1.0, 0.6, 0.4) ^a
	This work	(3.2, 2.2, 1.3, 0.8, 0.4) ^a

^aCorresponds to ages (0–0.5, 0.5–2.5, 2.5–7.5, 7.5–12.5, 12.5–18) years.

coefficients found in the literature and the corresponding mean value calculated in this work for a general neurovascular, adult and paediatric cardiovascular procedure. Overall, the results of this work are in good agreement with other publications.

4. Conclusions

A comprehensive framework for absorbed organ dose calculation in XA based on the dose-related data contained in RDSR has been presented. The framework provides a general approach, allowing any type of phantom model and method for radiation transport in the phantom to be used to estimate the absorbed dose to internal organs and to the skin. Furthermore, a novel method for reconstruction of the geometrical alignment of the patient's anatomy with the projected x-ray beam has been proposed and validated. The main advantages of the new approach are that it is patient- and procedure-specific and requires no user input or additional handling of the patient, such as clinical measurements or application of fiducial markers. This approach has been shown to be a major improvement over previous methods for reconstruction of the patient-beam alignment in the target organ region, i.e. the primarily irradiated body region and therefore the region of main concern.

The present work has demonstrated the means for systematic and fully automated calculation of absorbed organ doses on a patient-specific basis for XA procedures in routine clinical practice, something that has traditionally not been possible. Such calculations can be used to better understand the patient radiation exposure, which is invaluable for optimization of clinical methods and protocols. They further allow cumulative dose recording for individual patients, which will provide valuable data for epidemiological studies on the long-term harmful effects of low dose ionizing radiation.

Acknowledgments

This work is part of the XQuality project at Karolinska University Hospital in Stockholm, Sweden, which aims to improve patient and staff radiation safety in clinical practice. Partial funding was provided through the internal RDE fund at the Dept. of Medical Physics at Karolinska University Hospital.

Appendix A. The target-centric approach for reconstruction of the patient-beam alignment

The proposed algorithm for estimating the target organ position, $\mathbf{r}_{\text{target}}^{\text{TC}}$, is summarized in pseudocode in algorithm Appendix A.1, with the input RDSR data defined in table A1. In order to obtain $\mathbf{r}_{\text{target}}^{\text{TC}}$, the algorithm constructs the x-ray beam isocenter position relative to the head end of the table as a function of irradiation time, $\mathbf{r}_{\text{iso}}(t) = (x, y, z)$, and then solves equation (4) for $t \in \mathcal{X}$. Given that the x-ray beam isocenter position (\mathbf{r}_{b}) and the table head end position (\mathbf{r}_{t}) are expressed in terms of the same coordinate system, then \mathbf{r}_{iso} can for irradiation event i be defined as $\mathbf{r}_{\text{iso},i} = \mathbf{r}_{\text{b},i} - \mathbf{r}_{\text{t},i}$. $\mathbf{r}_{\text{iso}}(t)$ can thus be formulated as a step function defined as a linear combination of indicator functions,

$$\mathbf{r}_{\text{iso}}(t) = \sum_i \mathbf{r}_{\text{iso},i} 1_{\mathcal{T}_i}(t), \quad (\text{A.1})$$

where $1_{\mathcal{T}}(t)$ is the indicator function of a subset \mathcal{T} of irradiation times,

$$1_{\mathcal{T}}(t) = \begin{cases} 1 & \text{if } t \in \mathcal{T} \\ 0 & \text{if } t \notin \mathcal{T} \end{cases}. \quad (\text{A.2})$$

To improve the accuracy in estimated target organ position, the algorithm determines the set \mathcal{X} of irradiation times when the following constraints are considered. For neurovascular procedures only irradiation geometries corresponding to a target position within a lateral distance of d (25 cm in this work) from the table top head end are considered, i.e. $|z(t)| \leq d$. Also, since in some cases a substantial amount of fluoroscopy image guidance is carried out distal from the target region, only stationary acquisition irradiation events are considered, the exception being if no stationary acquisition irradiation events have been performed, in which case all events are considered.

Table A1. Definition of the input RDSR data for algorithm Appendix A.1.

Notation	Type	Description
\mathbf{r}_b	array of vectors for n irradiation events	x-ray beam isocenter position ^a
\mathbf{r}_t	array of vectors for n irradiation events	table top head end position ^a
w	array for n irradiation events	irradiation duration
A	array for n irradiation events	irradiation event type
s	string	study description

^a $(x, y, z) =$ (Along the table width direction, height direction, length direction).

Algorithm Appendix A.1.

Input: n -array \mathbf{r}_b , \mathbf{r}_t , w and A , string s

let $\mathbf{r}_{\text{iso},i} = \mathbf{r}_{b,i} - \mathbf{r}_{t,i}$, $w_0 = 0$

if $\exists i : A_i = \{\text{stationary acquisition}\}$ **then**

let $\mathcal{X} = \emptyset$ **else** let $\mathcal{X} = \{t \mid w_0 < t \leq \sum_{i=1}^n w_i\}$

end

for $i = 1$ **to** n **do**

let $\mathcal{T}_i \leftarrow \{t \mid w_{i-1} < t \leq w_{i-1} + w_i\}$

if $A_i = \{\text{stationary acquisition}\}$ **then**

let $\mathcal{X} \leftarrow \mathcal{X} \cup \mathcal{T}_i$

end

if $s = \{\text{neurovascular}\}$ **and** $|z_i| > d$ **then**

let $\mathcal{X} \leftarrow \mathcal{X} \setminus \mathcal{T}_i$

end

end

solve equation (4) with $\mathbf{r}_{\text{iso}}(t) = \sum_{i=1}^n \mathbf{r}_{\text{iso},i} 1_{\mathcal{T}_i}(t)$, given \mathcal{X} .

References

References

- Alm-Carlsson G, Dance D R, DeWerd L, Kramer H, Ng K, Pernicka F and Ortiz-Lopez P 2009 Dosimetry in diagnostic radiology: an international code of practice Technical Reports Series no 457 Vienna: International Atomic Energy Agency.
- Benmakhlouf H, Bouchard H, Fransson A and Andreo P 2011 Backscatter factors and mass energy-absorption coefficient ratios for diagnostic radiology dosimetry *Phys Med Biol* **56**(22), 7179–7204.
- Benmakhlouf H, Fransson A and Andreo P 2013 Influence of phantom thickness and material on the backscatter factors for diagnostic x-ray beam dosimetry *Phys Med Biol* **58**(2), 247–260.
- Birch R and Marshall M 1979 Computation of bremsstrahlung X-ray spectra and comparison with spectra measured with a Ge(Li) detector. *Phys Med Biol* **24**(3), 505–517.
- Chugh K, Dinu P, Bednarek D R, Wobschall D, Rudin S, Hoffmann K, Peterson R and Zeng M 2004 A computer-graphic display for real-time operator feedback during interventional x-ray procedures *Proc. SPIE* **5367**, 464–473.
- Compagnone G, Ortolani P, Domenichelli S, Ovi V, Califano G, Dall’Ara G and Marzocchi A

- 2011 Effective and equivalent organ doses in patients undergoing coronary angiography and percutaneous coronary intervention *Med Phys* **38**(4), 2168–2175.
- Cristy M and Eckerman K 1987 Specific absorbed fractions of energy at various ages from internal photon sources. I. Methods. Report/TM-8381/V1 Oak Ridge: Oak Ridge National Laboratory.
- den Boer A, de Feijter P J, Serruys P W and Roelandt J R 2001 Real-time quantification and display of skin radiation during coronary angiography and intervention *Circulation* **104**(15), 1779–1784.
- DICOM 2005 Supplement 94: Diagnostic x-ray radiation dose reporting (Dose SR) National Electrical Manufacturers Association (NEMA) Rosslyn, Virginia.
- Hubbell J H and Seltzer S M 2004 Tables of x-ray mass attenuation coefficients and mass energy-absorption coefficients Gaithersburgh, MD: National Institute of Standards and Technology. URL: <http://physics.nist.gov/xaamdi>
- IAEA 2009 IAEA Safety Reports Series 59: Establishing guidance levels in x ray guided medical interventional procedures: A pilot study.
- IAEA 2012 Joint position statement on the IAEA patient radiation exposure tracking Statement by the European Society of Radiology (ESR), U.S. Food and Drug Administration (FDA), International Atomic Energy Agency (IAEA), International Organization for Medical Physics (IOMP), International Society of Radiographers & Radiological Technologists (ISRRT), World Health Organization (WHO), Conference of Radiation Control Program Directors, USA (CRCPD). URL: <https://rpop.iaea.org/RPOP/RPoP/Content/Documents/Whitepapers/iaea-smart-card-position-st>
- ICRP 2007 ICRP Publication 103: The 2007 recommendations of the international commission on radiological protection *Ann. ICRP* **37**(2-4).
- ICRP 2012 ICRP Publication 118: Statement on tissue reactions / early and late effects of radiation in normal tissues and organs – Threshold doses for tissue reactions in a radiation protection context *Ann. ICRP* **41**(1/2).
- ICRU 2005 Appendix F: PCXMC: a PC-based Monte Carlo program for calculating organ doses for patients in medical x-ray examinations *J ICRU* **5**(2), 100–102.
- ICRU 2006 Patient dosimetry for x rays used in medical imaging *ICRU Report 74* .
- IEC 2010 Medical electrical equipment – Part 2-43: Particular requirements for the safety of x-ray equipment for interventional procedures *International Electrotechnical Commission 60601 2nd Ed.* .
- Johnson P B, Borrego D, Balter S, Johnson K, Siragusa D and Bolch W E 2011a Skin dose mapping for fluoroscopically guided interventions *Med Phys* **38**(10), 5490–5499.
- Johnson P B, Geyer A, Borrego D, Ficarrotta K, Johnson K and Bolch W E 2011b The impact of anthropometric patient-phantom matching on organ dose: A hybrid phantom study for fluoroscopy guided interventions *Med Phys* **38**(2), 1008–1017.
- Kagadis G C, Katsanos K, Karnabatidis D, Loudos G, Nikiforidis G C and Hendee W R 2012 Emerging technologies for image guidance and device navigation in interventional radiology *Med Phys* **39**(9), 5768–5781.
- Karambatsakidou A, Sahlgren B, Hansson B, Lidegran M and Fransson A 2009 Effective dose conversion factors in paediatric interventional cardiology *Br J Radiol* **82**(981), 748–755.
- Karambatsakidou A, Tornvall P, Saleh N, Chouliaras T, Löfberg P O and Fransson A 2005 Skin dose alarm levels in cardiac angiography procedures: is a single DAP value sufficient? *Br J Radiol* **78**(933), 803–809.
- Khodadadegan Y, Zhang M, Pavlicek W, Paden R G, Chong B, Schueler B A, Fetterly K A, Langer S G and Wu T 2011 Automatic monitoring of localized skin dose with fluoroscopic and interventional procedures *J Digit Imaging* **24**(4), 626–639.

- Manninen A L, Isokangas J M, Karttunen A, Siniluoto T and Nieminen M T 2012 A comparison of radiation exposure between diagnostic CTA and DSA examinations of cerebral and cervicocerebral vessels. *AJNR Am J Neuroradiol* **33**(11), 2038–2042.
- McCollough C H and Schueler B A 2000 Calculation of effective dose *Med Phys* **27**(5), 828–837.
- Miller D L, Balter S, Cole P E, Lu H T, Berenstein A, Albert R, Schueler B A, Georgia J D, Noonan P T, Russell E J, Malisch T W, Vogelzang R L, Geisinger M, Cardella J F, George J S, Miller, 3rd G L and Anderson J 2003 Radiation doses in interventional radiology procedures: the RAD-IR study: part II: skin dose *J Vasc Interv Radiol* **14**(8), 977–990.
- NCRP 2009 Ionizing radiation exposure of the population of the United States NCRP Report No. 160 Bethesda, MD: National Council on Radiation Protection and Measurements.
- NEMA 2015 Digital Imaging and Communications in Medicine (DICOM) Part 16: Content Mapping Resource. PS3.16-2015a *National Electrical Manufacturers Association (NEMA)* .
- Poludniowski G G 2007 Calculation of x-ray spectra emerging from an x-ray tube. Part II. X-ray production and filtration in x-ray targets. *Med Phys* **34**(6), 2175–2186.
- Poludniowski G G and Evans P M 2007 Calculation of x-ray spectra emerging from an x-ray tube. Part I. Electron penetration characteristics in x-ray targets. *Med Phys* **34**(6), 2164–2174.
- Schlattl H, Zankl M, Hausleiter J and Hoeschen C 2007 Local organ dose conversion coefficients for angiographic examinations of coronary arteries *Phys Med Biol* **52**(15), 4393–4408.
- Servomaa A and Tapiovaara M 1998 Organ dose calculation in medical x ray examinations by the program PCXMC *Radiation Protection Dosimetry* **80**(1-3), 213–219.
- Theodorakou C and Horrocks J A 2003 A study on radiation doses and irradiated areas in cerebral embolisation *Br J Radiol* **76**(908), 546–552.
- Vano E, Gonzalez L, Ten J I, Fernandez J M, Guibelalde E and Macaya C 2001 Skin dose and dose-area product values for interventional cardiology procedures *Br J Radiol* **74**(877), 48–55.
- Xu X G 2014 An exponential growth of computational phantom research in radiation protection, imaging, and radiotherapy: a review of the fifty-year history. *Phys Med Biol* **59**(18), R233–R302.